

A Sci-Viz Reconstruction and Analysis of the 1755 Lisbon Tsunami

Diogo Silva¹, Frederico Afonso¹, Tomás Pereira¹

¹*Master in Advanced Computing, University of Minho, Braga, Portugal*

Abstract

The 1755 Lisbon earthquake and tsunami were among the most destructive natural disasters in European history, yet their hydrodynamic behaviour remains poorly constrained due to the lack of direct observations. This work presents a scientific visualization driven study of the 1755 tsunami, combining large scale numerical modelling with post processing and representative near field flow analysis.

Tsunami propagation from the Horseshoe Fault is simulated using the GeoClaw framework, supported by high-resolution bathymetry. Wave propagation and coastal amplification are analyzed using gauge-based mareograms, maximum wave height maps, and ParaView visualizations.

To explore near-shore dynamics within the Tagus Estuary, representative OpenFOAM simulations are performed using tsunami induced inflow conditions derived from the GeoClaw results. While not intended as an exact reconstruction, these simulations illustrate physically plausible mechanisms such as coherent rotational flow and vortex shedding under extreme transient forcing.

Overall, this work highlights how scientific visualization can enhance the interpretation of tsunami simulations, linking numerical results with physical insight and historical evidence to better understand extreme coastal events.

Keywords: 1755 Lisbon tsunami, Scientific visualization, Tsunami modelling, GeoClaw, Okada, Horseshoe Fault, OpenFOAM, Adaptive mesh refinement, Estuarine hydrodynamics, ParaView

1. Introduction

The Azores-Gibraltar Transform Fault (AGTF), which marks the tectonic boundary between the Eurasian and African plates, is a major global source of high-magnitude earthquakes [1]. These seismic events often trigger powerful tsunamis, ranking among the world's most destructive natural phenomena. Throughout the last century, this region has produced several significant events,

Email addresses: pg61444@alunos.uminho.pt (Diogo Silva), pg59786@alunos.uminho.pt (Frederico Afonso), pg59810@alunos.uminho.pt (Tomás Pereira)

including the 1941 Gloria Fault earthquake [2] and the 1969 Horseshoe event [3], with magnitudes reaching or exceeding 8.0 M_w .

Among these geological events, the 1755 Lisbon earthquake and tsunami stand out as one of the most significant natural disasters on record. Over the last century, collaborative research has built a consensus regarding the potential geological causes and the specific sites where the rupture likely originated. As shown in previous studies, the Marquês de Pombal Fault (MPF) or the Horseshoe Fault (HSF) could be the sources of this Lisbon disaster [4, 5]. Among the potential sources, the Gorringe Bank [4] is the most prominent feature on this seabed and is known for recurring large-magnitude earthquakes [6]. While all these geological structures can be used to model the tsunami due to their proximity and shared characteristics, we opted for the Horseshoe Fault (HSF), as it is widely recognized for its accuracy in near-field simulations of the 1755 event.

In this work, we present a visualization-oriented analysis of the 1755 Lisbon tsunami. Our approach follows a strict methodology aligned with the scientific visualization pipeline. Since existing literature lacks simulations using ParaView [7] for this specific event, we propose various visualization techniques, validating and comparing our results against the current works in this field.

This study elevates tsunami simulation by providing a real-time, immersive visualization of the phenomenon’s progression. To visualize a tsunami, we consider different approaches that map all the dynamics before, during and after the impact.

2. Methodology

The foundation of this study is a rigorous multi-phase methodology. Phase one involves a critical re-evaluation of the 1755 event, contrasting established historical records with contemporary geophysical models. By analyzing the different geographic details, we validate our choice for this simulation on grounded knowledge already established on literature.

Following the historical contextualization, we justify the selection of the GeoClaw [8] simulator as our numerical engine. GeoClaw addresses the computational challenges of large-scale tsunami modelling through its state-of-the-art Adaptive Mesh Refinement (AMR). This feature is particularly beneficial for coastal geological phenomena, as it dynamically increases grid resolution in areas of interest—such as the advancing wave front and complex coastal bathymetry—while maintaining a coarser mesh in the open ocean. This approach optimizes computational resources without compromising the precision required to simulate the intricate inundation patterns of Lisbon’s 1755 event.

At the core of this research, we perform an extensive analysis of the results through advanced visualization techniques. To provide a comprehensive understanding of the phenomenon, we visualize the tsunami dynamics across multiple scales and dimensions, thereby validating the numerical outcomes with graphical representations. Figure 1 highlights this methodology process, showing three distinct phases to achieve our final results.

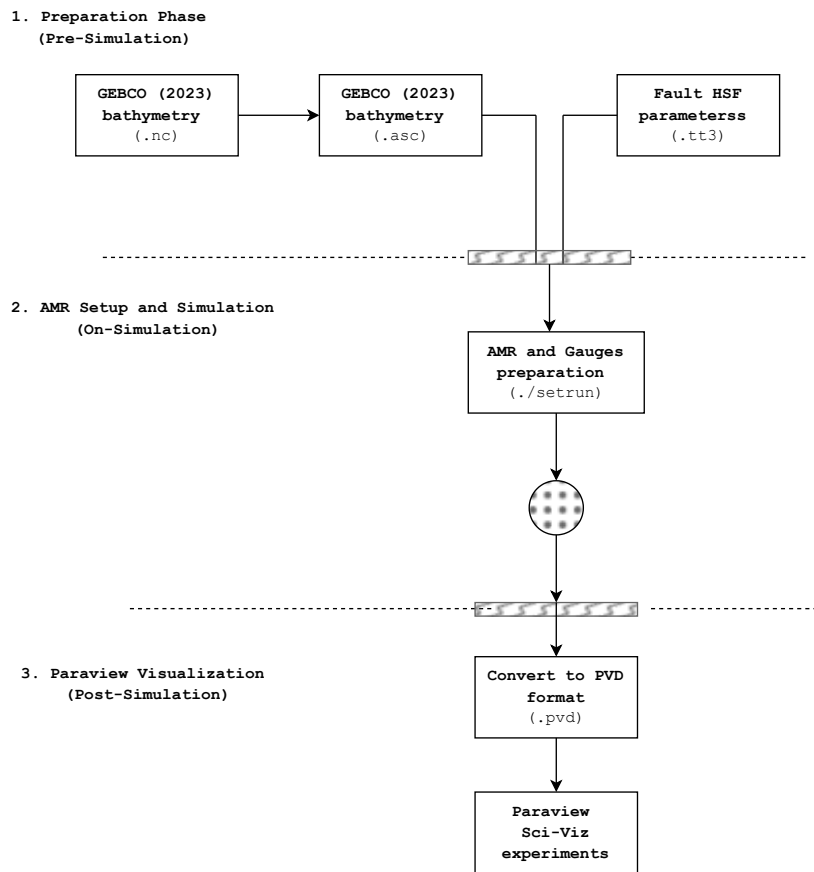


Figure 1: Pipeline of actions from data gathering to having a high-fidelity visualization on Paraview of 1755 Tsunami

3. Experimental Setup

The computational framework was deployed across various systems to accommodate different simulation scales. The results presented in this report were obtained using a 12th Gen Intel(R) Core(TM) i7-1260P processor (more details available at Table 1. Given that high-resolution tsunami simulations are computationally intensive, we leveraged OpenMP to exploit multi-threading capabilities, ensuring maximum utilization of the available processor cores.

Additionally, we designed a version to exploit Deucalion resources using the ARM partition. Geoclaw does not support MPI natively, which would be really advantageous in a supercomputer setting.

Table 1: Hardware specifications of the computational device used to simulate the 1755 Lisbon tsunami.

Feature	Specification
Manufacturer	Intel
Model	12th Gen Intel(R) Core(TM) i7-1260P
Architecture (SoC)	x86_64
Cores / Threads	12 / 16
Sockets	1
Frequency	4.7 GHz

4. Tsunami Modelling

4.1. Bathymetric data visualization

Before generating the simulation data using GeoClaw, we retrieved the bathymetric data to meet the requirements of our study specification. To this end, high-resolution bathymetric data were retrieved from the GEBCO 2023 DTM model.

Since the GeoClaw simulator utilizes Adaptive Mesh Refinement (AMR), we implemented a multi-scale approach. Three distinct bathymetric maps were extracted: Figure 2 shows a coarse-resolution snapshot covering the entire computational domain, a medium-scale transition grid for enhanced wave propagation accuracy, and a high-resolution sub-domain focused on the Tagus Estuary and downtown Lisbon for fine-scale inundation analysis.

The source of rupture utilized to simulate the 1755 tsunami was the Horseshoe Fault. Similar simulations like the one we realized report expected magnitudes of $8.3 M_w$

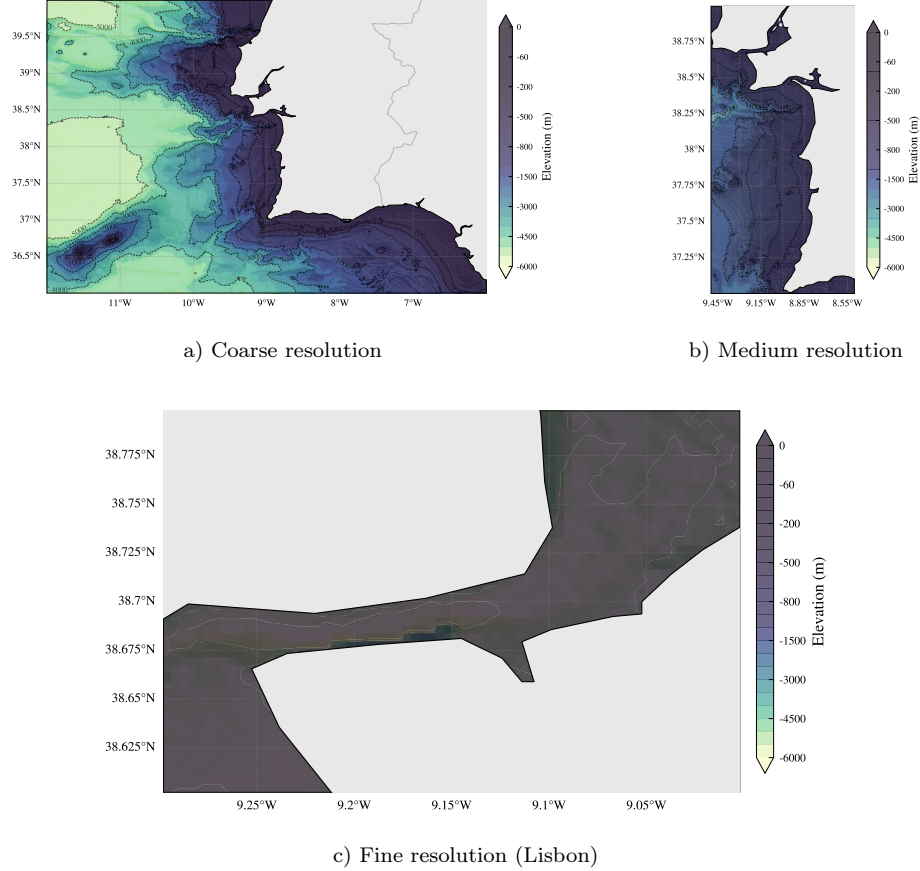


Figure 2: Bathymetric datasets used in the simulation. (a) Coarse domain of the North Atlantic; (b) Medium resolution grid; (c) High-resolution detail of the Tagus Estuary.

The geographical locations of the Marquês de Pombal (36.54°N , 9.89°W) and Horseshoe (35.74°N , 9.91°W) faults are highlighted on the coarse-resolution bathymetric map, representing the primary seismic sources we considered in our study.

4.2. Finding Horseshoe Fault Parameters and Okada Model

Following the bathymetric assessment, the source parameters for the Horseshoe fault were established. The simulation was configured using established geophysical values to ensure a realistic representation of the seismic event [5, 9]. The specific parameters utilized for the Horseshoe fault model are summarized in Table 2.

Table 2: Seismic source parameters for the Horseshoe (HSF) fault model used in the simulation.

Parameter	Value	Unit
Epicenter Longitude	-9.91	°W
Epicenter Latitude	35.74	°N
Strike (ϕ)	42.1	°
Dip (δ)	35	°
Rake (λ)	90	°
Slip (u)	10.7	m
Length (L)	165	km
Width (W)	70	km
Depth (d)	4	km

Before simulating, we had to use the Okada [10] model, available in GeoClaw, to find the initial displacements on the surface caused by the fault tectonic movement.

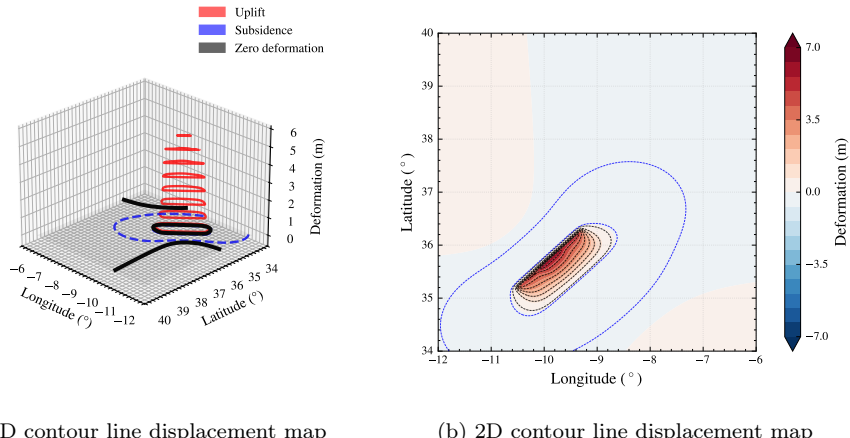


Figure 3: Initial seafloor deformation for the Horseshoe Fault (HSF) scenario calculated via Okada model: (a) 3D surface view; (b) 2D vertical displacement distribution.

Looking at Figure 3, we can see a clear vertical uplift concentrated along the Northwest axis. This seafloor displacement, which reaches about 6 meters, is the result of the Okada model using the Horseshoe Fault parameters from Table 2. Around this uplifted area, the blue zones represent the subsidence caused by the earthquake's crustal deformation. This 'dipolar' shape is exactly what is expected from a thrust-faulting mechanism. Furthermore, the way the contour lines are stretched shows that the tsunami energy is being directed perpendicularly [11] to the fault strike, pointing straight toward the Portuguese coast as the simulation begins.

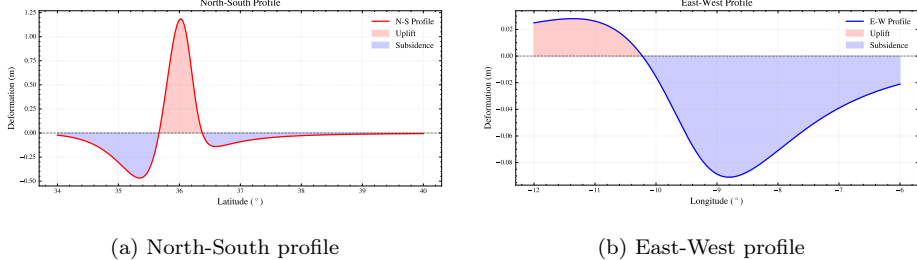


Figure 4: Distinct geographic profiles on Horseshoe Fault (HSF): (a) North-South fault displacement profile; (b) East-West fault displacement profile

Figure 4 confirms that deformation along the fault has two distinct profiles. It's clear that along the North axis, the fault had a major tendency to uplift. Even though Figure 3 doesn't make it clear that subsidence is primarily directed towards the east, now we can see that the Horseshoe fault is drenched towards the east side, which is consistent with the findings of Omira et al. [4].

Additionally, the magnitude of the generated earthquake was calculated, resulting on a $8.27 M_w$ seismic event [4, 5, 12].

4.3. Simulation Environment

To simulate this natural phenomenon, we utilized GeoClaw, which solves the Non-Linear Shallow Water Equations. The software employs finite volume methods to discretize these equations and produce a robust numerical solution.

According to the official documentation of GeoClaw [8], in its core, it solves the next set of equations:

$$\frac{\partial h}{\partial t} + \frac{\partial hu}{\partial x} + \frac{\partial hv}{\partial y} = 0 \quad (1)$$

$$\frac{\partial hu}{\partial t} + \frac{\partial(hu^2 + \frac{1}{2}gh^2)}{\partial x} + \frac{\partial huv}{\partial y} = -ghB_x - Du \quad (2)$$

$$\frac{\partial hv}{\partial t} + \frac{\partial huv}{\partial x} + \frac{\partial(hv^2 + \frac{1}{2}gh^2)}{\partial y} = -ghB_y - Dv \quad (3)$$

where $u(x, y, t)$ and $v(x, y, t)$ are the depth-averaged velocities along both directions in a two-dimensional plane. If both terms $D(u, v, t)$ and $B(x, y, t)$, which represent drag forces and bathymetry, respectively, were to be zero, which is not the case, the three equations would state the conservation of mass and momentum.

Even while both bathymetry and thrust fault are initial conditions required to solve the Non-Linear Shallow Water Equations, they are not sufficient to describe the physical behavior of this phenomena. To ensure the simulation is correct under a limited domain area, we defined transparent boundary conditions, which avoid a ricochet of the wave. Additionally, the Monotonized Central

(MC) limiter was employed to provide a robust balance between numerical dissipation and dispersion. This ensures that steep gradients at the wavefront remain stable, avoiding oscillations. Frictional resistance was parameterized using a uniform Manning's coefficient of $n = 0.025$ [5, 8].

The GeoClaw framework allows the use of gauges, tantamount to sensors, which track the tsunami momentum along different time-steps of the simulation on a specific site. Multiple stationary gauges were used along the ocean at different sites to track different patterns.

5. Simulation Results and Discussion

The simulation achieved a total wall clock time of 1.67 hours. Analysis of the runtime distribution shows that the core integration steps accounted for the majority of the computational effort, particularly within the finest AMR refinement levels (third and fourth level). Upon testing different configurations, we conclude that it is key to fine-tune AMR levels to avoid extreme regridding and memory-consuming operations.

Using the information extracted from the different gauge sites, we constructed various mareograms [13] to gain a better understanding of the surface elevation behaviour over time. At the Horseshoe Fault, Figure 5, the initial fault thrust is visible within the first 10 minutes of the occurrence. In this zone, the surface elevation peaks at nearly 1.25 meters, not so precise as the 3 meters registered by Omira et al. [4], since we have used a smaller level of refinement.

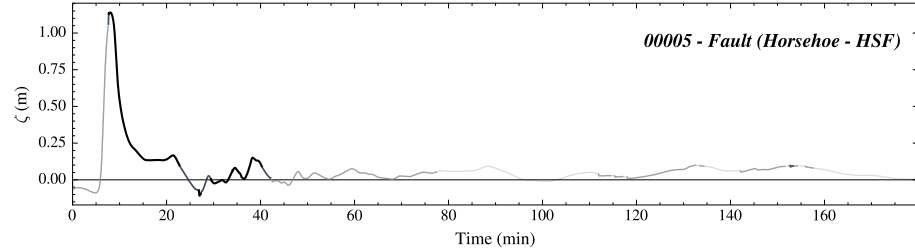


Figure 5: Water surface elevation (ζ) time series at the Horseshoe Fault source zone (Gauge 5). The instantaneous displacement at $t = 0$ reflects the initial seafloor deformation. Line grayscale gradients indicate the adaptive mesh refinement (AMR) levels active during the simulation.

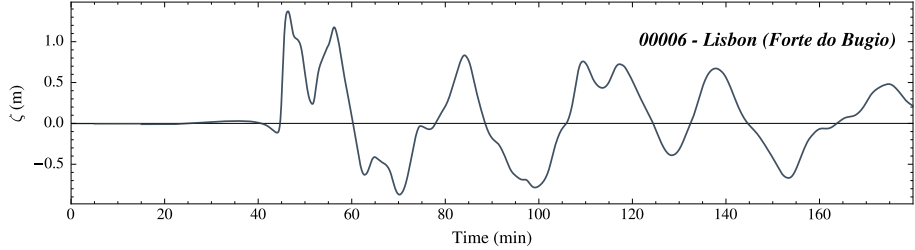


Figure 6: Water surface elevation (ζ) time series at the Forte do Bugio (Lisbon) (Gauge 6). Near $t = 40$, it's visible a big surface elevation is visible, reflecting the arrival of the tsunami in the Lisbon coastal zones.

Conversely, near Lisbon at the Forte do Bugio gauge, the marigram reveals a characteristic oscillatory wave train. This pattern illustrates the succession of multiple wave crests and troughs typical of a tsunami event. As the simulation progresses, the amplitude gradually attenuates, reflecting the energy dissipation as the waves interact with the shallow bathymetry of the Tagus estuary. Since Baptista et al. [14] observed a 5m crest at Forte do Bugio, we consider this gauge study fallible since it uses a smaller refinement, and the placement of the gauge could not catch the shallow bathymetry near Bugio.

From another perspective, we calculated the Maximum Wave Height (MWH) because gauge data alone does not fully show what happened during the entire simulation. As shown in Figure 7, Sagres and the Algarve are heavily impacted by the tsunami, with maximum wave heights reaching nearly 5 m in these zones. In Lisbon, where the adaptive mesh refinement (AMR) was most focused, certain areas show a MWH between 3 m and 4 m. The difference between the two regions is mainly because Lisbon is much further from the source (HSF) than the South of Portugal. Additionally, since wave peaks are highly sensitive to grid resolution, these values in Lisbon should be seen as conservative; a higher refinement along the wave's path would likely result in even higher values in this area [14].

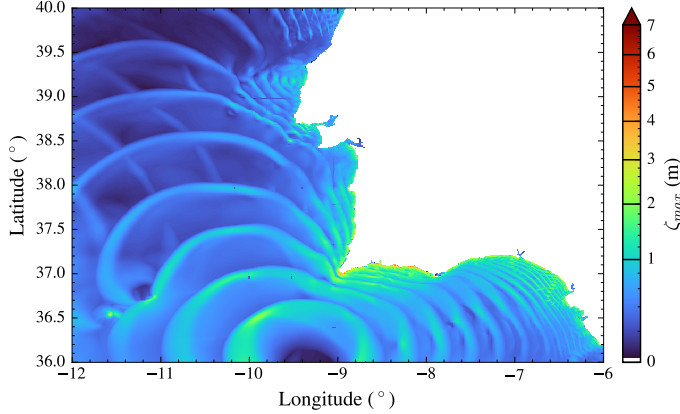


Figure 7: The Maximum Wave Height, ζ_{max} , for the full domain of study. The figure reveals near shore sites tend to suffer more of the impact of bigger waves.

6. 1755 Tsunami Sci-Viz with Paraview

Beyond validation, such complex scientific problems require different kinds of visualizations. Using Sci-Viz tools like Paraview, it's possible to see an animation of the event, which allows the visualization of wave patterns that could be missing in an analytical analysis of the problem.

The raw results from GeoClaw, generated in ASCII format, were not natively supported initially by the Paraview framework. To overcome this we decided to port ASCII to Paraview data (.pvд). In Figure 8 we show the impact of using AMR in tsunami simulations, revealing the differences in precision across different cells. At $t = 0$, there is a clear distinction between grid refinement levels. In this case, the darker blue areas represent a level-two refinement, capturing the Horseshoe Fault and its surrounding area.

6.1. Scientific visualization of Flow Velocity

The simulator used provides linear momentum of the waves on both longitudinal and transversal directions. With these values it's possible to extract flow velocity at a certain location and time with the following equation:

$$v = \sqrt{\left(\frac{hu}{h}\right)^2 + \left(\frac{hv}{h}\right)^2} \quad (4)$$

where h is the water depth, and, u and v are the velocities along the two-dimensional grid.

By exporting the flow velocity to ParaView, we were able to track the flow evolution during wave propagation from the source to the coast. At $t = 0$ min, from Figure 9, as expected, the flow velocity is zero since the simulation has just initialized. After the first recorded timestep at $t = 5$ min, the Horseshoe Fault displacement has already generated a wave, reaching a maximum flow

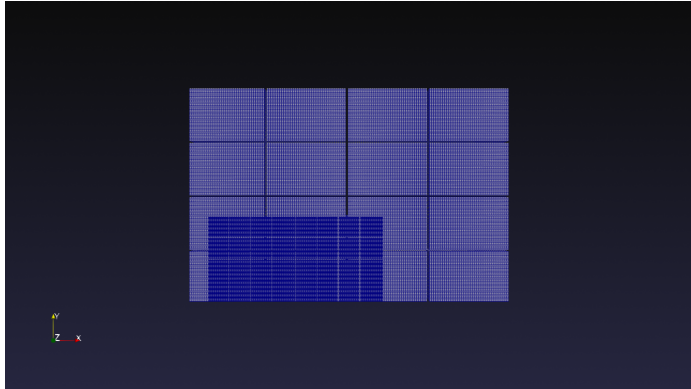


Figure 8: Adaptive mesh refinement visualization at the initial timestep, using 'Surface with Edges'. Darker colors enlighten smaller distances between adjacent cells.

velocity (v) of approximately 0.2 m/s. During the rest of the simulation, it is clear that the potential energy in deeper ocean is being converted into kinetic energy in shallower waters[15]. This happens due to higher friction between water particles; this is the reason tsunamis can become so destructive.

From the analytical results and figure inspection, it is evident that the maximum flow velocity is achieved after 135 minutes of simulation, reaching approximately 11 m/s near the Gulf of Cadiz.

6.2. 6.2 Bathymetry 3D Visualization

Finally, we provide a more comprehensive visualization of the surrounding bathymetry of Portugal costal area.

Since ParaView treats AMR patches as separate blocks, a Merge Blocks filter was applied to unify the patches into a single object. This allowed for uniform data manipulation across all resolution levels. To generate a 3D representation, a Warp by Scalar filter was applied to the bathymetry, creating a consistent 3D mold of both the Portuguese mainland and the Atlantic basin.

Looking at Figure 10, the two crest zones in the sea, which sit relatively high, almost at sea level, are the Gorringe Bank. From this three-dimensional approach, we can see that sites near land are definitely shallower, which makes behaviors like those in velocity or MWH appear in tsunamis.

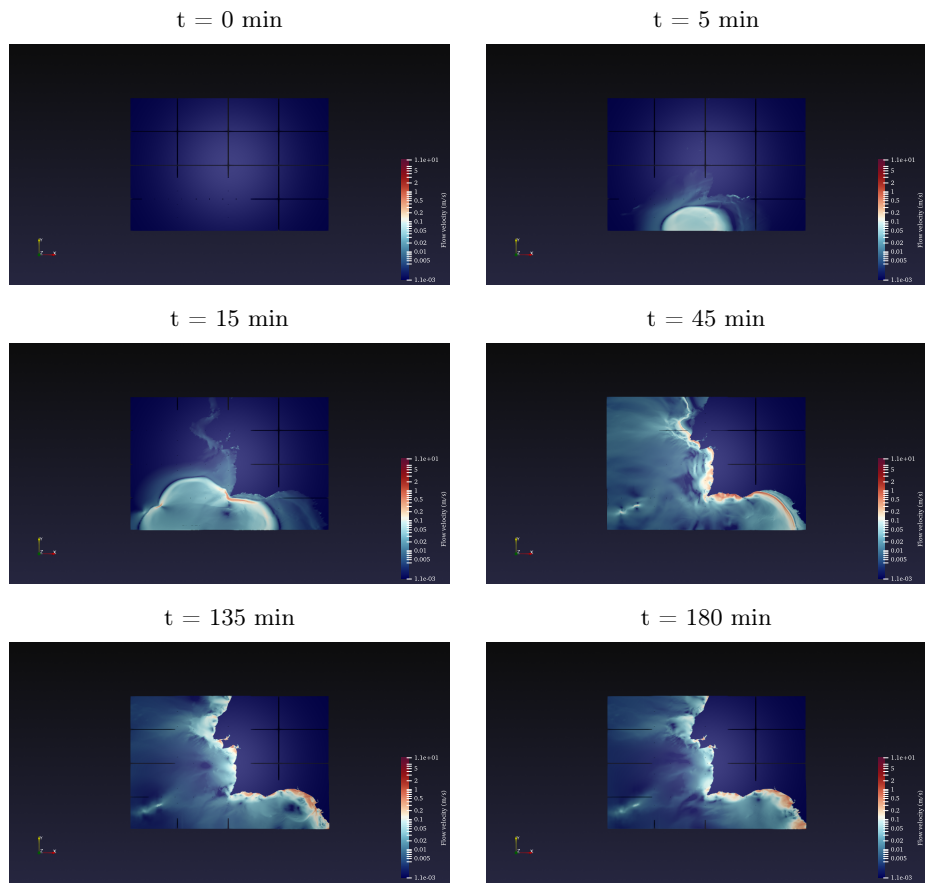


Figure 9: Spatiotemporal evolution of the tsunami flow velocity magnitude (v) at different time steps (in minutes).

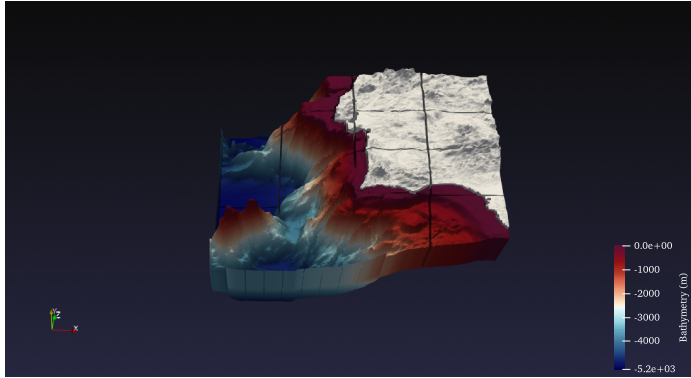


Figure 10: Three-dimensional bathymetry visualization using Paraview tool. Hotter colours represent bathymetry near sea level.

7. Further Discussions - Vortex Shedding and Coherent Structures in the Tagus Estuary

7.1. Physical Context and Motivation

Beyond large-scale tsunami wave propagation, near-shore and estuarine dynamics are strongly governed by local hydrodynamic instabilities induced by geometric confinement and complex bathymetry. Narrow channels, abrupt depth variations, and coastal constrictions can promote flow separation and the formation of coherent vortical structures, significantly altering local velocity fields and hydrodynamic loads.

One of the most widely studied manifestations of such instabilities is the Bénard–von Kármán vortex street, typically observed in unsteady flows past bluff bodies at moderate Reynolds numbers. While classical vortex shedding is often investigated under controlled laboratory conditions, analogous mechanisms may emerge in natural estuarine systems during extreme transient events, including tsunamis. Historical descriptions of the 1755 Lisbon tsunami report intense rotational currents, violent water motion, and vessel displacement within the Tagus River, suggesting the presence of strong vortical dynamics.

Motivated by these historical observations, this work explores whether tsunami-driven inflow interacting with the constricted geometry of the Tagus Estuary can *plausibly* generate organized vortex shedding-like patterns. Due to the absence of time-resolved hydrodynamic measurements from 1755 and the impossibility of reconstructing exact boundary conditions, the present analysis does not claim to reproduce the historical flow field. Instead, it aims to provide a physically consistent and representative scenario illustrating mechanisms that *could have occurred* under extreme tsunami forcing.

7.2. Numerical Approach and Visualization Methodology

The vortex shedding analysis was conducted using OpenFOAM, which solves the incompressible Navier–Stokes equations and enables explicit resolution of

velocity gradients and rotational structures. Because no direct observational data from the 1755 event exist, the OpenFOAM simulations were not driven by real-time measurements but rather by representative inflow conditions derived from the large-scale tsunami wave fields generated with GeoClaw.

This coupling strategy ensures consistency between far-field tsunami propagation and near-field estuarine dynamics, while acknowledging that the imposed boundary conditions constitute an idealized approximation. The resulting flow fields should therefore be interpreted as *physically plausible realizations* rather than exact reconstructions.

Post-processing and scientific visualization were performed in ParaView following a structured Sci-Viz pipeline. The vertical component of vorticity was computed as

$$\omega_z = \frac{\partial v}{\partial x} - \frac{\partial u}{\partial y}, \quad (5)$$

and used as the primary diagnostic to identify coherent rotational structures.

To enhance interpretability, additional vector-based visualizations were generated: (i) stream tracer animations to reveal recirculation zones and the unsteady advection of vortices, and (ii) sparse velocity glyph fields to locally inspect directional alternation and shear-layer development without trajectory integration. These complementary visualizations (glyphs and stream tracers) are provided in the project repository for transparency and reproducibility.

7.3. Results and Discussion

The OpenFOAM simulations reveal the formation of alternating vortical structures downstream of constricted regions within the Tagus Estuary during the tsunami inflow phase. As water accelerates through the narrow entrance, strong shear layers develop near lateral boundaries, leading to flow separation and the emergence of coherent vortices with alternating sign of vorticity.

These structures exhibit spatial organization consistent with a vortex shedding-like regime at geophysical scale, driven by transient tsunami forcing rather than steady inflow. While the precise timing, size, and intensity of these vortices cannot be validated against historical measurements, their emergence is consistent with fundamental fluid-dynamical principles and with qualitative historical descriptions of violent rotational currents in the estuary.

From a historical interpretation standpoint, the results should be viewed as illustrative rather than reconstructive: they demonstrate how extreme tsunami-induced inflow *could* generate large-scale rotational dynamics capable of amplifying local damage, rather than asserting that the simulated vortices exactly matched those of the 1755 event.

7.4. Relation to Classical Vortex Shedding

While classical Bénard–von Kármán vortex streets are typically associated with steady flow past isolated bluff bodies, the mechanisms observed here share key similarities: flow separation, alternating vortex formation, and downstream

advection. The principal distinction lies in the transient, wave-driven nature of tsunami forcing and the complex natural geometry of the Tagus Estuary.

This analogy supports the use of vortex shedding theory as a conceptual framework for interpreting extreme estuarine flow phenomena, while maintaining appropriate caution regarding historical reconstruction. Scientific visualization thus plays a central role in connecting physically grounded numerical experimentation with historical narratives and qualitative evidence.

As shown in Fig. 11, the representative tsunami inflow generates alternating vorticity structures downstream of estuarine constrictions. A zoomed region-of-interest highlighting coherent vortices is presented in Fig. 12. Additional stream tracer and glyph-based visualizations are available in the project repository.

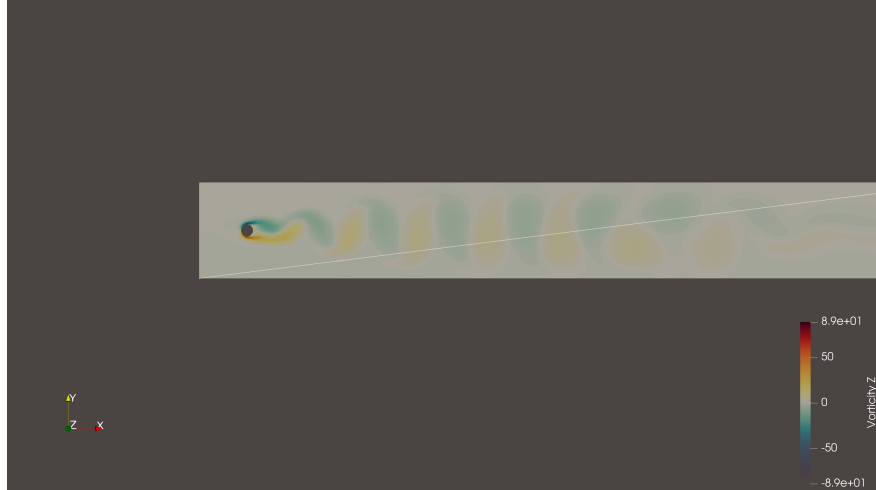


Figure 11: Instantaneous vertical vorticity field (ω_z) obtained from a representative OpenFOAM simulation of tsunami-driven flow in the Tagus Estuary. The alternating regions of positive and negative vorticity illustrate a physically plausible vortex shedding-like response under extreme inflow conditions, rather than a direct reconstruction of the 1755 event.

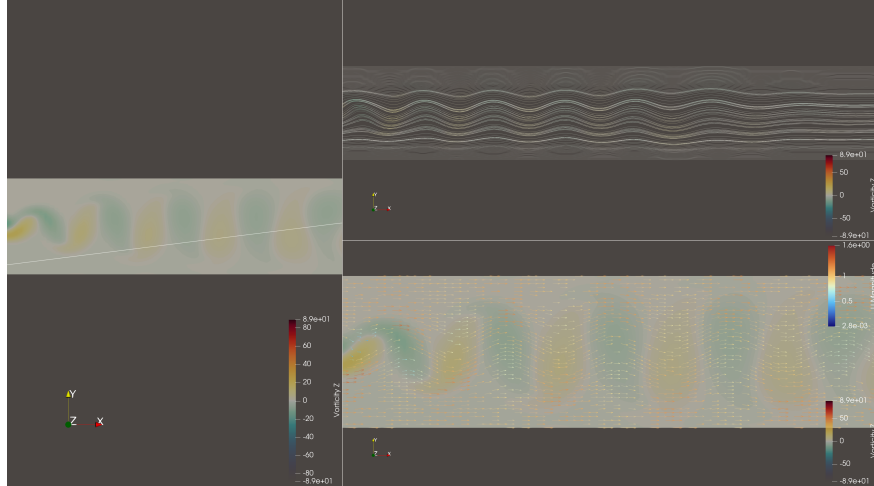


Figure 12: Overview of the scientific visualization outputs generated in ParaView for the representative OpenFOAM simulation. The figure aggregates multiple views, including vorticity fields, stream tracer representations, and velocity-based visual encodings, illustrating complementary perspectives on the coherent flow structures induced by tsunami-driven inflow in the Tagus Estuary.

8. Conclusions and Future Work

The results of our tsunami simulation are highly dependent on grid refinement. While current literature often utilizes a 10-meter resolution, such precision was computationally prohibitive given our available hardware. Despite this lower resolution, the fundamental physics of the tsunami and its propagation dynamics remained consistent and viable, capturing the essential behavior of the event.

The utilization of ParaView was essential for observing and animating the 3D dynamics of the tsunami, providing insights that simple analytical plotting cannot offer. While this approach has not yet been fully adopted in current literature, its superior presentation capabilities help bridge the gap between complex numerical data and physical understanding, making the results more accessible and intuitive.

In the future, we consider doing a more intricate analysis on wave run-up and its effect on population, evaluating the impact of height and velocity on Mercalli intensity scales. Lastly, we consider it crucial to port this simulation to MPI using multiple nodes to accelerate deeper mesh refinements.

References

- [1] R. Barkan, U. S. ten Brink, J. Lin, Far field tsunami simulations of the 1755 lisbon earthquake: Implications for tsunami hazard to the u.s. east coast and the caribbean, *Marine Geology* 264 (1–2) (2009) 109–122. doi: 10.1016/j.margeo.2008.10.010.

- [2] M. A. Baptista, J. M. Miranda, J. Batlló, F. Lisboa, J. Luis, R. Maciá, New study on the 1941 Gloria Fault earthquake and tsunami, *Natural Hazards and Earth System Sciences* 16 (8) (2016) 1967–1977. doi:10.5194/nhess-16-1967-2016.
- [3] M. A. Baptista, J. M. Miranda, R. Omira, The 28th February 1969 Earthquake and Tsunami in the Atlantic Iberian Margin, *Pure and Applied Geophysics* 182 (4) (2025) 1363–1380. doi:10.1007/s00024-025-03689-z.
- [4] R. Omira, M. A. Baptista, L. Matias, J. M. Miranda, C. Catita, F. Carrilho, E. A. Toto, Design of a Sea-level Tsunami Detection Network for the Gulf of Cadiz, *Natural Hazards and Earth System Sciences* 9 (4) (2009) 1327–1338. doi:10.5194/nhess-9-1327-2009.
- [5] R. Omira, M. A. Baptista, J. M. Miranda, Evaluating Tsunami Impact on the Gulf of Cadiz Coast (Northeast Atlantic), *Pure and Applied Geophysics* 168 (6) (2011) 1033–1043. doi:10.1007/s00024-010-0217-7.
- [6] R. Sartori, L. Torelli, N. Zitellini, D. Peis, E. Lodolo, Eastern segment of the Azores-Gibraltar line (central-eastern Atlantic): an oceanic plate boundary with diffuse compressional deformation, *Geology* 22 (6) (1994) 555–558. doi:10.1130/0091-7613(1994)022<0555:ESOTAG>2.3.CO;2.
- [7] J. Ahrens, B. Geveci, C. Law, ParaView Guide: A Parallel Visualization Application, Kitware, Inc., available at <https://www.paraview.org/> (2005).
- [8] M. J. Berger, D. L. George, R. J. LeVeque, K. T. Mandli, The GeoClaw software for depth-averaged flows with adaptive refinement, *Advances in Water Resources* 34 (9) (2011) 1195–1206. doi:10.1016/j.advwatres.2011.02.016.
- [9] K. Aki, P. G. Richards, Quantitative Seismology, 2nd Edition, University Science Books, Sausalito, California, 2002.
- [10] Y. Okada, Surface deformation due to shear and tensile faults in a half-space, *Bulletin of the Seismological Society of America* 75 (4) (1985) 1135–1154. doi:10.1785/BSSA0750041135.
- [11] V. V. Titov, H. O. Mofjeld, F. I. Gonzalez, J. C. Newman, Offshore forecasting of Alaska-Aleutian subduction zone tsunamis in Hawaii, Tech. rep., NOAA Technical Memorandum, ERL PMEL-114, Seattle, Washington, available at <https://www.pmel.noaa.gov/pubs/PDF/tito2032/tito2032.pdf> (1999).
- [12] K. Abe, Size of great earthquakes of 1837–1974 inferred from tsunami data, *Journal of Geophysical Research: Solid Earth* 84 (B4) (1979) 1561–1568. doi:10.1029/JB084iB04p01561.

- [13] A. Yankovsky, S. Dovgal, Numerical simulation of propagation of tsunami waves in the black sea caused by the earthquake on 12 september, 1927, in: 18th International Multidisciplinary Scientific GeoConference SGEM 2018, Science and Technologies in Geology, Exploration and Mining, SGEM, Albenia, Bulgaria, 2018. doi:10.5593/sgem2018/1.2.
- [14] M. A. Baptista, J. M. Miranda, R. Omira, C. Antunes, Potential inundation of Lisbon downtown by a 1755-like tsunami, *Natural Hazards and Earth System Sciences* 11 (12) (2011) 3319–3326. doi:10.5194/nhess-11-3319-2011.
- [15] F. E. Camfield, Tsunami engineering, Special Report Special Report No. 6, Coastal Engineering Research Center, Vicksburg, MS (1980).